SISSA

Implementation of Maxwell's equations in the reconstruction of the magnetic field in the g−2 storage ring

View the article online for updates and enhancements.

IOP ebooks™

Bringing you innovative digital publishing with leading voices to create your essential collection of books in STEM research.

Start exploring the collection - download the first chapter of every title for free.

Implementation of Maxwell's equations in the reconstruction of the magnetic field in the $g - 2$ storage ring

G.T. Bodwin,[a] **H.S. Chung**[a,b,c,1] **and J. Repond**[a]

[a]*High Energy Physics Division, Argonne National Laboratory,*
9700 S. Cass. Ave, Lemont, IL 60439, U.S.A.

[b]*Physik-Department, Technische Universität München,*
James-Franck-Str. 1, 85748 Garching, Germany

[c]*Theory Department, CERN,*
1211 Geneva 23, Switzerland

E-mail: heesok.chung@tum.de

ABSTRACT: We present a method for implementing the constraints that are implied by Maxwell's equations in fits to measurements of the magnetic field in the muon storage ring of the $g - 2$ experiment. The method that we use makes use of toroidal-harmonic solutions of Laplace's equation. We point out that the fitting problem can be approximated well as a linear-algebra problem. We have devised an efficient algorithm for the linear-algebra problem that makes it possible to find a solution for 10^5 data points and 10^4 harmonics in less than an hour on a present-day desktop computer. We illustrate our method by applying it to some preliminary measurements of the magnetic field in the $g - 2$ storage ring.

---

[1]Corresponding author.

Contents

1 Introduction

Precise knowledge of the magnetic field inside the muon storage ring is of paramount importance for the measurements of the muon anomalous magnetic moment $(g-2)$ that will be made by the Fermilab experiment E989 [1]. The primary method of measurement of the magnetic field, which utilizes a circular array of nuclear-magnetic-resonance (NMR) probes, determines only the magnitude of the magnetic field, not its direction. Ancillary measurements using Hall probes have been used to obtain information about components of the field that are orthogonal to its average direction [2].

Additional information about the magnetic field can be obtained by making use of the constraints that are implied by Maxwell's equations. Since the inside of the muon storage ring is a vacuum, Maxwell's equations for the magnetic field $\boldsymbol{B}$ become

$$\boldsymbol{\nabla} \cdot \boldsymbol{B} = \boldsymbol{0}, \tag{1.1a}$$

$$\boldsymbol{\nabla} \times \boldsymbol{B} = \boldsymbol{0}. \tag{1.1b}$$

Because the magnetic field in the ring is almost entirely in the z (vertical) direction, the NMR-probe measurements give information about the gradients of B_z. That information, in combination with eqs. (1.1), allows one to compute the gradients of the field components in the transverse directions,

which can be used to check the Hall-probe measurements. In the $g - 2$ experiment, the main effect of the transverse fields is to induce oscillations of the beam in the transverse direction, and so knowledge of the transverse fields provides a useful consistency test of the observations of beam dynamics. In a proposed measurement of the muon's electric dipole moment (EDM), knowledge of the transverse fields may play a more significant role, facilitating a reduction of measurement systematic uncertainties.

As a first step in analyzing the ring magnetic field, we make use of the fact that the magnetic field is almost uniform in direction and magnitude inside the storage ring. Therefore, we can write $\boldsymbol{B}$ as a sum of the uniform field $\langle B \rangle \hat{z}$ and a fluctuation $\boldsymbol{B}_{\mathrm{f}}$:

$$\boldsymbol{B} = \langle B \rangle \hat{z} + \boldsymbol{B}_{\mathrm{f}}, \tag{1.2}$$

where $\hat{z}$ is a unit vector in the direction of the average of the $\boldsymbol{B}$ field over the active volume of the storage ring. For the E989 ring, $\hat{z}$ is very close to the vertical direction. We choose $\langle B \rangle$ to be about the same size as the average magnetic field strength. The precise value of $\langle B \rangle$ is unimportant, as small changes in $\langle B \rangle$ can be absorbed into $\boldsymbol{B}_{\mathrm{f}}$. However, as we will see, it is crucial to our analysis that $\boldsymbol{B}_{\mathrm{f}}$ be small compared with $\langle B \rangle$.

Since the uniform field $\langle B \rangle \hat{z}$ satisfies Maxwell's equations in vacuum, so does the fluctuation $\boldsymbol{B}_{\mathrm{f}}$. The equation $\boldsymbol{\nabla} \times \boldsymbol{B}_{\mathrm{f}} = \boldsymbol{0}$ implies that $\boldsymbol{B}_{\mathrm{f}}$ can be written as a gradient of a scalar function V, which satisfies

$$\boldsymbol{\nabla} V = \boldsymbol{B}_{\mathrm{f}}, \tag{1.3a}$$

$$\nabla^2 V = 0. \tag{1.3b}$$

Eq. (1.3b), which follows from $\boldsymbol{\nabla} \cdot \boldsymbol{B}_{\mathrm{f}} = 0$, is Laplace's equation.

The region of validity of eq. (1.3b) can be an issue because the single-valuedness of V relies on eq. (1.1b), through Stokes' theorem. For the E989 muon storage ring, there are no currents through the plane of the ring at radii that lie inside the outermost part of the vacuum chamber. Consequently, V is single-valued inside the vacuum chamber.

In this paper, we implement Maxwell's equations in fits to the NMR measurements of the storage-ring magnetic field by expressing the fitting function as a sum of solutions of Maxwell's equations. We do this by writing V as an expansion in a complete set of solutions of Laplace's equation (harmonic functions). In particular, we use toroidal harmonics as the basis functions, since their coordinate geometry is particularly well matched to the geometry of a toroidal storage ring. We exclude the large constant field $\langle B \rangle \hat{z}$ from the toroidal-harmonic fit, as it would be necessary to go to a very high order in the toroidal harmonics in order to achieve a fit to $\langle B \rangle \hat{z}$ of sufficient accuracy.

The fitting problem for the $g - 2$ ring involves a large number of data points and harmonics, and, as we will see, is underconstrained. Hence, the fitting problem, in its original form, is quite formidable. We have developed several simplifications/reorganizations of the fitting algorithm that make the fitting problem computationally tractable.

We have applied our fitting algorithm to preliminary data from the $g - 2$ trolley runs. While these data do not reflect the ultimate precision of the NMR measurements or the ultimate quality of the $g - 2$ storage-ring magnetic field, they serve to illustrate the fitting procedure and its utility.

The remainder of this paper is organized as follows. In section 2 we describe the toroidal-harmonic expansion of the magnetic field. In section 3 we outline our method for fitting the toroidal

harmonic series to the data. Here we describe the algorithmic improvements that we have made. Section 4 contains some examples of the application of our fitting procedure to some of the early NMR magnetic-field data. Finally, in section 5, we summarize our results.

2   Use of toroidal harmonics to implement Maxwell's equations

Toroidal-harmonic solutions of Laplace's equation of been known for many years [3, 4]. Many of the modern applications of expansions of magnetic fields in toroidal harmonics have focused on magnetic fields in tokamaks [5–7]. A theoretical study of expansions of magnetic fields in spherical, cylindrical, and toroidal harmonics was given in ref. [8]. In that study, toroidal-harmonic expansions for ideal toroidal magnets were discussed, and numerical fitting of order ten toroidal harmonics was carried out for the situation in which fields could be sampled uniformly in the angles of the toroidal coordinate system. To our knowledge, our work is the first to address the use of thousands of toroidal harmonics in fitting nearly uniform magnetic fields to high precision. The methods that we employ do not require uniform sampling of the fields in the angles of the toroidal coordinate system.

The expansion of a vacuum magnetic field in toroidal harmonics is discussed in detail in ref. [5]. Here, we present the essential features of that expansion.

Toroidal coordinates (ζ, η, ϕ) are given in terms of Cartesian coordinates (x, y, z) as follows:

$$x = R\frac{\sinh \zeta}{\cosh \zeta - \cos \eta} \cos \phi, \tag{2.1a}$$

$$y = R\frac{\sinh \zeta}{\cosh \zeta - \cos \eta} \sin \phi, \tag{2.1b}$$

$$z = R\frac{\sin \eta}{\cosh \zeta - \cos \eta}. \tag{2.1c}$$

Here, $0 \le \zeta < \infty$, $0 \le \eta < 2\pi$, and $0 \le \phi < 2\pi$. ϕ is the usual azimuthal angle about the z axis, with $\phi = 0$ corresponding to the x axis. R is a constant that has a dimension of length. The surface of constant ζ is a torus of major and minor radii of $R/\tanh \zeta$ and $R/\sinh \zeta$, respectively. ($\zeta \to \infty$ corresponds to a circle of radius R in the $x - y$ plane. $\zeta \to 0$ corresponds to the z axis for η nonzero and to one or more of x, y, and z becoming infinite when η goes to zero, depending on the relative speeds with which ζ and η go to zero.) The poloidal angle η specifies, for each circular ϕ slice of the torus, the position on the circle. The surface of constant η is a sphere of radius $R/\sin \eta$, whose origin is at $x = y = 0$ and $z = R/\tan \eta$. The toroidal coordinates are illustrated in figure 1.

Although there is some freedom in choosing the value of R, it should not be too different from the radius of the storage ring, so that a torus defined by a constant ζ roughly coincides with the interior of the storage ring. For numerical calculations, R should be adjusted so that the points of interest do not lie exactly on the circle of radius R in the $x - y$ plane; otherwise, one encounters $\zeta = \infty$ in coordinate transformations. In practice, we take R to be 0.99993 times the $g - 2$ ring radius, which corresponds to a shift of 0.5 mm from the ring center. This leads to a maximum value of $\zeta = 10.26$ for the central NMR probe in the $g - 2$ trolley. That value is easily accommodated by the available numerical dynamic range in our computation. We have tried varying R in the range 0.997118–1.00274 times the $g - 2$ ring radius, and find that that variation affects our results at the level of a few ppb or less, which is negligible in comparison with other uncertainties.
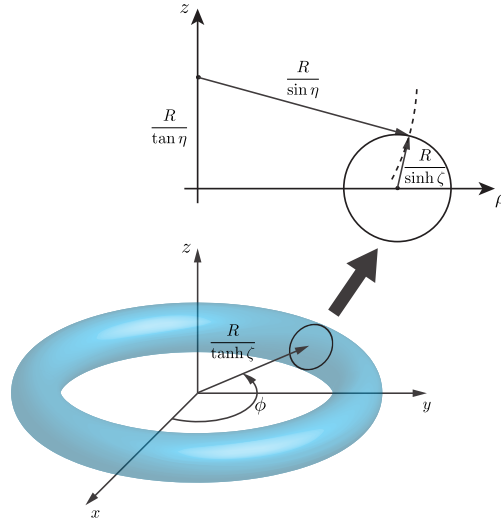
Figure 1. Illustration of toroidal coordinates. The surface of constant ζ is a torus of major and minor radii of $R/\tanh\zeta$ and $R/\sinh\zeta$, respectively, whose center is located at $x = y = z = 0$. The surface of constant η is a sphere of radius $R/\sin\eta$, whose origin is at $x = y = 0$ and $z = R/\tan\eta$.

The general solution to Laplace's equation, which is found by using the technique of separation of variables in toroidal coordinates, is a linear combination of the following toroidal harmonics, which are defined for nonnegative integers m and n by

$$\sqrt{\cosh\zeta - \cos\eta}\, P^n_{m-1/2}(\cosh\zeta)\cos(m\eta)\cos(n\phi), \tag{2.2a}$$

$$\sqrt{\cosh\zeta - \cos\eta}\, P^n_{m-1/2}(\cosh\zeta)\cos(m\eta)\sin(n\phi), \tag{2.2b}$$

$$\sqrt{\cosh\zeta - \cos\eta}\, P^n_{m-1/2}(\cosh\zeta)\sin(m\eta)\cos(n\phi), \tag{2.2c}$$

$$\sqrt{\cosh\zeta - \cos\eta}\, P^n_{m-1/2}(\cosh\zeta)\sin(m\eta)\sin(n\phi), \tag{2.2d}$$

$$\sqrt{\cosh\zeta - \cos\eta}\, Q^n_{m-1/2}(\cosh\zeta)\cos(m\eta)\cos(n\phi), \tag{2.2e}$$

$$\sqrt{\cosh\zeta - \cos\eta}\, Q^n_{m-1/2}(\cosh\zeta)\cos(m\eta)\sin(n\phi), \tag{2.2f}$$

$$\sqrt{\cosh\zeta - \cos\eta}\, Q^n_{m-1/2}(\cosh\zeta)\sin(m\eta)\cos(n\phi), \tag{2.2g}$$

$$\sqrt{\cosh\zeta - \cos\eta}\, Q^n_{m-1/2}(\cosh\zeta)\sin(m\eta)\sin(n\phi). \tag{2.2h}$$

Here, the toroidal functions $P^n_{m-1/2}(\cosh\zeta)$ and $Q^n_{m-1/2}(\cosh\zeta)$ are half-integer Legendre functions of the first and second kind, respectively. $P^n_{m-1/2}(\cosh\zeta)$ and $Q^n_{m-1/2}(\cosh\zeta)$ can be expressed in

terms of the hypergeometric function as [5, 9]

$$
\begin{aligned}
P^n_{m-1/2}(\cosh \zeta) &= \frac{\Gamma\left(m+n+\frac{1}{2}\right)}{2^n n! \, \Gamma\left(m-n+\frac{1}{2}\right)} \tanh^n \zeta \, \cosh^{m-1/2} \zeta \\
&\times {}_2F_1\left[\frac{1}{2}\left(n-m+\frac{1}{2}\right), \frac{1}{2}\left(n-m+\frac{3}{2}\right); n+1; \tanh^2 \zeta\right],
\end{aligned}
\tag{2.3a}
$$

$$
\begin{aligned}
Q^n_{m-1/2}(\cosh \zeta) &= \sqrt{\frac{\pi}{2}} \frac{\Gamma\left(m+n+\frac{1}{2}\right)}{2^m \Gamma(m+1)} \frac{\tanh^n \zeta}{\cosh^{m+1/2} \zeta} \\
&\times {}_2F_1\left[\frac{1}{2}\left(m+n+\frac{1}{2}\right), \frac{1}{2}\left(m+n+\frac{3}{2}\right); m+1; \operatorname{sech}^2 \zeta\right].
\end{aligned}
\tag{2.3b}
$$

The $P^n_{m-1/2}(\cosh \zeta)$ correspond to the solutions that are singular at $\zeta \to \infty$, and the $Q^n_{m-1/2}(\cosh \zeta)$ correspond to the solutions that are regular at $\zeta \to \infty$. Therefore, harmonics containing $P^n_{m-1/2}(\cosh \zeta)$ correspond to contributions from sources in the interior of the ring, and harmonics containing $Q^n_{m-1/2}(\cosh \zeta)$ correspond to contributions from sources outside the ring. We use the forms in eq. (2.3) for our numerical computations.[1]

In practical calculations, it is necessary to work with a finite number of harmonics. This may result in significant inaccuracies if the potential V is not single valued.[2] The potential V may not be single valued when the region of space that satisfies eq. (1.3b) is multiply connected. For example, the condition $V(\zeta, \eta + 2\pi, \phi) = V(\zeta, \eta, \phi)$ can be spoiled if there is a current that flows inside the ring because the line integral $\oint_C d\boldsymbol{x} \cdot \boldsymbol{B}$ along a closed curve C does not vanish if C encloses a nonzero net current. For the muon storage ring, the condition $V(\zeta, \eta + 2\pi, \phi) = V(\zeta, \eta, \phi)$ holds because, in the absence of the muon beam itself, the interior of the ring is a vacuum. The condition $V(\zeta, \eta, \phi + 2\pi) = V(\zeta, \eta, \phi)$ is ensured by the fact that $\oint_C d\boldsymbol{x} \cdot \boldsymbol{B} = 0$, where the path C is on the interior of the ring and encloses the z axis. The vanishing of this line integral follows from the fact that no net current flows through the plane of the ring at radii that lie inside the outermost part of the vacuum chamber.

We set the cutoffs for m and n to be M and N, respectively. In order to eliminate solutions that correspond to currents that pass through the plane of the storage ring at radii that lie inside the outermost part of the vacuum chamber, we exclude the harmonics $P^n_{m-1/2}(\cosh \zeta)$ from the solution. Then, we obtain

$$
\begin{aligned}
V(\zeta, \eta, \phi) &= \sqrt{\cosh \zeta - \cos \eta} \sum_{m=0}^{M} \sum_{n=0}^{N} \frac{Q^n_{m-1/2}(\cosh \zeta)}{Q^n_{m-1/2}(\cosh \zeta_0)} \\
&\times \left[C^{mn}_{\mathrm{CC}} \cos(m\eta) \cos(n\phi) + C^{mn}_{\mathrm{CS}} \cos(m\eta) \sin(n\phi) \right. \\
&\left. + C^{mn}_{\mathrm{SC}} \sin(m\eta) \cos(n\phi) + C^{mn}_{\mathrm{SS}} \sin(m\eta) \sin(n\phi) \right],
\end{aligned}
\tag{2.4}
$$

where, for numerical stability, we divide each toroidal harmonic by $Q^n_{m-1/2}(\cosh \zeta_0)$, so that $Q^n_{m-1/2}(\cosh \zeta)/Q^n_{m-1/2}(\cosh \zeta_0)$ is always order one when $\zeta \approx \zeta_0$. This approach allows us to

---

[1]We have tested the Mathematica built-in hypergeometric functions numerically against the algorithm in the appendix of ref. [5], for which truncation errors are given, and find good agreement over the range of indices m and n that we use.

[2]For example, the Fourier expansion for the function $f(\theta) = \theta$ for $0 \le \theta \le 2\pi$ does not converge uniformly.

avoid the computation of gamma functions with large arguments in eq. (2.3). There is some arbitrariness in the choice of ζ_0. An appropriate choice for ζ_0 is one such that $R/\tanh \zeta_0$, and $R/\sinh \zeta_0$, are approximately equal to the major and minor radii, respectively, of the storage ring.

Once we have fixed the $(2M + 1) \times (2N + 1)$ constants[3] C_{CC}^{mn}, C_{CS}^{mn}, C_{SC}^{mn}, and C_{SS}^{mn}, we can give an approximate reconstruction of the magnetic field in the storage ring. The magnetic field components are given by the gradient of eq. (2.4). The magnetic field can be written in terms of cylindrical basis vectors as

$$\boldsymbol{B} = \langle B \rangle \hat{z} + \boldsymbol{\nabla} V = B_\rho \hat{\boldsymbol{\rho}} + B_z \hat{z} + B_\phi \hat{\boldsymbol{\phi}}, \tag{2.5}$$

where [5]

$$B_\rho = \frac{\sinh \zeta}{R} \left(\frac{1 - \cosh \zeta \cos \eta}{\sinh \zeta} \frac{\partial V}{\partial \zeta} - \sin \eta \frac{\partial V}{\partial \eta} \right), \tag{2.6a}$$

$$B_z = \langle B \rangle + \frac{\sinh \zeta}{R} \left(-\sin \eta \frac{\partial V}{\partial \zeta} - \frac{1 - \cosh \zeta \cos \eta}{\sinh \zeta} \frac{\partial V}{\partial \eta} \right), \tag{2.6b}$$

$$B_\phi = \frac{\cosh \zeta - \cos \eta}{R \sinh \zeta} \frac{\partial V}{\partial \phi}. \tag{2.6c}$$

Hereafter, we refer to B_ρ, B_z, and B_ϕ as radial, vertical, and longitudinal fields, respectively.

One might ask whether other coordinate systems in which Laplace's equation is separable, such as spherical coordinates or cylindrical coordinates, could be used to analyze the magnetic field of the $g - 2$ ring. In principle, such coordinate systems are also valid for this purpose. However, the resulting mis-match between the coordinate system and the ring geometry would make the expansions in the corresponding harmonics converge slowly.

One might also ask whether one should sample the magnetic field uniformly over the toroidal coordinate system or uniformly over the plane of each slice in azimuthal angle, as is done in the $g - 2$ experiment. While uniform sampling over the toroidal coordinate system might lead to some simple relationships between the sample values and the constants $C_{CC}^{mn}, C_{CS}^{mn}, C_{SC}^{mn}, C_{SS}^{mn}$, it would not reduce the number of harmonics that are required to achieve a given precision. More importantly, for the $g - 2$ experiment, the key issue is the uniformity of the field over the entire fiducial volume, and this is best assessed with a uniform sampling of the field over the plane of each slice in azimuthal angle.

3 Fitting the toroidal-harmonic series to data

Now we discuss the strategy to constrain the magnetic field by comparing the expressions in eqs. (2.4) and (2.6) with the measured magnetic field.

3.1 Linearization of the problem

We determine the constants C_{CC}^{mn}, C_{CS}^{mn}, C_{SC}^{mn}, and C_{SS}^{mn} by fitting the expressions in eqs. (2.4) and (2.6) to the measured magnetic field strengths B_{measured}. The most straightforward way to do this is to find a set of constants that minimizes the sum of squares of residuals S, which is defined by

$$S = \sum_{p=1}^{N_{\text{data}}} \left[B_{\text{measured}}(\boldsymbol{x}_p) - |\langle B \rangle \hat{z} + \boldsymbol{\nabla} V(\boldsymbol{x}_p)| \right]^2, \tag{3.1}$$

---

[3]Since $\sin 0 = 0$, $C_{CS}^{m0}, C_{SC}^{0n}, C_{SS}^{0n}$ and C_{SS}^{m0} do not appear in eq. (2.4).

where $\boldsymbol{x}_p$ is the position at which the measurement of the p'th data point is made, N_{data} is the total number of measurements, and V is given by eq. (2.4).

Although minimization of S is a general method with which to fit the data, it is not feasible to carry out in practice, especially when M, N, and N_{data} are large. Each component of $\boldsymbol{B} = B_\rho \hat{\boldsymbol{\rho}} + B_z \hat{\boldsymbol{z}} + B_\phi \hat{\boldsymbol{\phi}}$ at a given position in space is a linear polynomial that depends on $N_{\text{constants}} \equiv (2M + 1) \times (2N + 1)$ constants. Then, the field strength $|\boldsymbol{B}| = \sqrt{B_\rho^2 + B_z^2 + B_\phi^2}$ that appears in eq. (3.1) is a square root of a quadratic polynomial that depends on $N_{\text{constants}}$ constants, which can contain up to $\frac{1}{2}(N_{\text{constants}} + 1)(N_{\text{constants}} + 2)$ terms. Since the sum of the square roots of different polynomials does not, in general, simplify, the number of terms in S is about $\frac{1}{2}N_{\text{constants}}^2 N_{\text{data}}$. In the case of our fits to the storage-ring field data, $N_{\text{constants}}$ is typically of order 10^3 and N_{data} is typically of order 10^6. Hence, the computation of S becomes very compute-time intensive.

In order to simplify the fitting problem, we take the following approach. We expand the magnitude of the field strength

$$|\boldsymbol{B}| = \sqrt{\langle B \rangle^2 + 2\langle B \rangle \hat{\boldsymbol{z}} \cdot \boldsymbol{B}_{\text{f}} + \boldsymbol{B}_{\text{f}}^2}. \tag{3.2}$$

in powers of $\boldsymbol{B}_{\text{f}}$:

$$|\boldsymbol{B}| = \sqrt{(\langle B \rangle + \hat{\boldsymbol{z}} \cdot \boldsymbol{B}_{\text{f}})^2 + (\hat{\boldsymbol{\rho}} \cdot \boldsymbol{B}_{\text{f}})^2 + (\hat{\boldsymbol{\phi}} \cdot \boldsymbol{B}_{\text{f}})^2} = \langle B \rangle + \hat{\boldsymbol{z}} \cdot \boldsymbol{B}_{\text{f}} + O\left(\boldsymbol{B}_{\text{f}}^2/\langle B \rangle\right). \tag{3.3}$$

Since the transverse components of the magnetic field in the $g - 2$ storage ring are typically about 100 ppm, the corrections beyond linear order are of order 0.01 ppm, which is of the same order as the nominal error in the NMR-probe measurements. Therefore, we can reasonably ignore the corrections beyond the linear order. In the linear approximation, we have $|\boldsymbol{B}| = B_z$. Therefore, in the linear approximation, the sum of squares of residuals becomes

$$S_L = \sum_{p=1}^{N_{\text{data}}} \left[B_{\text{measured}}(\boldsymbol{x}_p) - B_z(\boldsymbol{x}_p) \right]^2. \tag{3.4}$$

B_z is a linear polynomial containing $N_{\text{constants}}$ constants. Then, each term in the sum in eq. (3.4) is a quadratic polynomial containing $N_{\text{constants}}$ constants, which can have up to $\frac{1}{2}(N_{\text{constants}}+1)(N_{\text{constants}}+2)$ terms. When we add polynomials to perform the sum in eq. (3.4), we can simply add the coefficients numerically. Thus, the number of terms in S_L is $\frac{1}{2}(N_{\text{constants}}+1)(N_{\text{constants}}+2)$. This is a factor of $1/N_{\text{data}}$ smaller than the number of terms in S. By minimizing S_L, we find an approximate solution to the following set of equations, which, in general, is overconstrained:

$$B_z(\boldsymbol{x}_p) = B_{\text{measured}}(\boldsymbol{x}_p), \tag{3.5a}$$

where the measurement index p takes on the values $p = 1, 2, \ldots, N_{\text{data}}$. Since $B_z(\boldsymbol{x}_p)$ is a linear polynomial that contains $N_{\text{constants}}$ constants, eq. (3.5a) can be rewritten as

$$\sum_{i=1}^{N_{\text{constants}}} \frac{\partial B_z(\boldsymbol{x}_p)}{\partial c_i} c_i = B_{\text{measured}}(\boldsymbol{x}_p) - \langle B \rangle. \tag{3.5b}$$

where $c_1, c_2, \ldots, c_{N_{\text{constants}}}$ denote the constants C_{CC}^{mn}, C_{CS}^{mn}, C_{SC}^{mn}, and C_{SS}^{mn}.

A further advantage of the linear approximation is that it reduces the minimization problem to a linear-algebra problem. Since S_L is a sum of squares of linear polynomials, it is bounded from below, and, if S_L has one local minimum, then the local minimum coincides with the global minimum. The condition for a local minimum is

$$\frac{\partial S_L}{\partial c_i} = 0, \tag{3.6}$$

for all $i = 1, 2, \ldots, N_{\text{constants}}$. Since S_L is a quadratic polynomial, the left side of eq. (3.6) is a linear polynomial. Therefore, eq. (3.6) can be rewritten as

$$\sum_{j=1}^{N_{\text{constants}}} A_{ij} c_j = b_i, \tag{3.7}$$

where

$$A_{ij} \equiv \frac{1}{2} \frac{\partial^2 S_L}{\partial c_i \partial c_j} = \sum_{p=1}^{N_{\text{data}}} \frac{\partial B_z(\boldsymbol{x}_p)}{\partial c_i} \frac{\partial B_z(\boldsymbol{x}_p)}{\partial c_j}, \tag{3.8a}$$

$$b_i \equiv -\frac{1}{2} \frac{\partial S_L}{\partial c_i} \bigg|_{c_j = 0 \text{ for all } j} = \sum_{p=1}^{N_{\text{data}}} [B_{\text{measured}}(\boldsymbol{x}_p) - \langle B \rangle] \frac{\partial B_z(\boldsymbol{x}_p)}{\partial c_i}. \tag{3.8b}$$

The square matrix A and the column matrix b are numerical and do not depend on the c's. A is symmetric and positive semidefinite. Eq. (3.7) has a unique solution if A is positive definite, i.e., if A has no vanishing eigenvalues. However, as we will explain in the next section, this is not the case in our application. That is, our linear least-squares problem is underconstrained.

There are many well developed methods for solving eq. (3.7). One such method is singular-value decomposition (SVD).[4] In this method, the expression $\partial B_z(\boldsymbol{x}_p)/\partial c_i$ on the left side of eq. (3.5b) is regarded as a matrix with indices p and i. Then SVD is used to find the pseudoinverse[5] of that matrix. A solution to the linear least squares problem is obtained by applying the pseudoinverse matrix to the right side of eq. (3.5b). Again, as we will explain in the next section, the solution of the linear least-squares problem is not unique.

The SVD method is particularly well suited to non-unique linear least-squares problems, such as ours, because it allows one to identify the zero eigenvalues of the matrix A in eq. (3.7). However, we have found that the direct application of the SVD method to solve eq. (3.7) is impractical for several reasons. First, the appearance of large numbers of different linear combinations of unconstrained c_i's makes it difficult to identify those linear combinations and to sequester them. Second, the computation, when it can be carried out, is very intensive computationally. Finally, the data display fluctuations between measurements at different azimuthal angles that are much larger than differences between the measurements of the various probes at a fixed azimuthal angle. In order to deal with these issues, we make a further rearrangement of the linear least-squares problem. In this re-arrangement, which we describe in detail in section 3.3, we first analyze the azimuthal dependence of the data, using Fourier decomposition, and then analyze the ρ-z of the Fourier coefficients in order to determine the toroidal-harmonic coefficients.

---

[4]See, for example, ref. [10].

[5]Here, and throughout this paper, we use the term "pseudoinverse" to mean the Moore-Penrose inverse of a matrix [11–14]. See ref. [10] for a discussion of the pseudoinverse in the context of SVD.

3.2 Underconstrained nature of the linear least-squares problem

In the linear approximation, the measured magnetic fields constrain only B_z directly. B_ρ and B_ϕ are constrained indirectly from knowledge of B_z and the vacuum Maxwell's equations. From $\boldsymbol{\nabla} \cdot \boldsymbol{B} = 0$ and $\boldsymbol{\nabla} \times \boldsymbol{B} = \boldsymbol{0}$, we obtain the following relations

$$\frac{\partial B_z}{\partial z} = -\frac{\partial B_\rho}{\partial \rho} - \frac{1}{\rho} B_\rho - \frac{1}{\rho} \frac{\partial B_\phi}{\partial \phi}, \tag{3.9a}$$

$$\frac{\partial B_z}{\partial \rho} = \frac{\partial B_\rho}{\partial z}, \tag{3.9b}$$

$$\frac{\partial B_z}{\partial \phi} = \rho \frac{\partial B_\phi}{\partial z}. \tag{3.9c}$$

Hence, once B_z is determined, the vertical gradients of the radial and longitudinal fields can be constrained. However, aside from the combination $\partial B_\rho/\partial \rho + \rho^{-1} B_\rho + \rho^{-1} \partial B_\phi/\partial \phi$, neither the field gradients in the radial or the longitudinal directions nor the absolute sizes of B_ρ and B_ϕ can be determined from B_z. This implies that a comparison of the expression for B_z with the measured magnetic field strengths cannot constrain all $(2M + 1) \times (2N + 1)$ constants C_{CC}^{mn}, C_{CS}^{mn}, C_{SC}^{mn}, and C_{SS}^{mn}. We will deal with the underconstrained nature of the fits by making use of singular-value decomposition (SVD) to solve eq. (3.5b). In this method, the unconstrained modes correspond to zero eigenvalues of the matrix A. We discard the associated eigenvectors from the solution. In practice, this is done by setting to zero any inverse eigenvalues in the SVD pseudoinverse matrix that correspond to eigenvalues that are smaller than a "tolerance" ϵ. While this results in a well-defined solution to the fitting problem, it is important to recognize that this is just one of an infinite number of solutions to this underconstrained problem. That means that this solution must be interpreted with care, recognizing that only the gradients with respect to z of the radial field B_ρ and the longitudinal field B_ϕ are fully determined by the constraints that are given in eqs. (3.9).

3.3 Further rearrangement of the linear least-squares problem

As we have mentioned, even the linearized fitting problem can be formidable to solve computationally, since it may involve on the order of 10^5 data points and 10^4 harmonics. We can considerably improve the computational efficiency by carrying out the analysis in steps. The first step is to express the ϕ dependence of the data for each NMR probe in terms of a Fourier series. The second step is to use the Fourier-series coefficients for all of the probes to determine the coefficients of the toroidal harmonics. The first step in this approach relies on three facts: (1) the data from each NMR trolley probe are a function of ϕ alone (at fixed ρ and z), (2) the toroidal-harmonic expansion of the potential V depends on ϕ only through sine and cosine factors in each harmonic, and (3) B_z does not involve azimuthal derivatives of V.

3.3.1 Fourier series for the probe data

In order to display the sine and cosine factors in the harmonics explicitly, we write

$$V_C(\zeta, \eta, n) = \sqrt{\cosh\zeta - \cos\eta} \sum_{m=0}^{M} \frac{Q_{m-1/2}^n(\cosh\zeta)}{Q_{m-1/2}^n(\cosh\zeta_0)} \left[C_{CC}^{mn} \cos(m\eta) + C_{SC}^{mn} \sin(m\eta) \right], \quad (3.10a)$$

$$V_S(\zeta, \eta, n) = \sqrt{\cosh\zeta - \cos\eta} \sum_{m=0}^{M} \frac{Q_{m-1/2}^n(\cosh\zeta)}{Q_{m-1/2}^n(\cosh\zeta_0)} \left[C_{CS}^{mn} \cos(m\eta) + C_{SS}^{mn} \sin(m\eta) \right], \quad (3.10b)$$

so that

$$V(\zeta, \eta, \phi) = \sum_{n=0}^{N} [V_C(\zeta, \eta, n) \cos(n\phi) + V_S(\zeta, \eta, n) \sin(n\phi)]. \quad (3.11)$$

Applying eq. (2.6b) to eq. (3.11), we obtain

$$B_z(\zeta, \eta, \phi) = \langle B \rangle + \sum_{n=0}^{N} [B_C(\zeta, \eta, n) \cos(n\phi) + B_S(\zeta, \eta, n) \sin(n\phi)], \quad (3.12)$$

where

$$B_C(\zeta, \eta, n) = \frac{\sinh\zeta}{R} \left[-\sin\eta \frac{\partial V_C(\zeta, \eta, n)}{\partial \zeta} - \frac{1 - \cosh\zeta\cos\eta}{\sinh\zeta} \frac{\partial V_C(\zeta, \eta, n)}{\partial \eta} \right], \quad (3.13a)$$

$$B_S(\zeta, \eta, n) = \frac{\sinh\zeta}{R} \left[-\sin\eta \frac{\partial V_S(\zeta, \eta, n)}{\partial \zeta} - \frac{1 - \cosh\zeta\cos\eta}{\sinh\zeta} \frac{\partial V_S(\zeta, \eta, n)}{\partial \eta} \right]. \quad (3.13b)$$

Now we define a truncated Fourier series for each NMR probe that has the same form as the truncated Fourier series in eq. (3.12):

$$B_{\text{Fourier}}(q, \phi; N) = \sum_{n=0}^{N} [\beta(q, 2n; N) \cos(n\phi) + \beta(q, 2n+1; N) \sin(n\phi)]. \quad (3.14)$$

Here, the index q, which runs from 1 to N_{probe}, labels the NMR probe, whose ζ and η coordinates are ζ_q and η_q, respectively. Note that we retain the index N in the arguments of the coefficients β as a reminder that these coefficients depend on the order of truncation of the Fourier series.

3.3.2 Using the probe data to constrain the Fourier coefficients

A standard method for determining the coefficients of a Fourier series is to make use of the orthonormality relations for sines and cosines. In our case, application of these orthonormality relations would lead to the following equations for the Fourier coefficients $\beta(q, n; N)$:

$$\beta(q, 0; N) = \frac{1}{2\pi} \int_{-\pi}^{+\pi} d\phi \, B_{\text{Fourier}}(q, \phi; N), \quad (3.15a)$$

$$\beta(q, 2n; N) = \frac{1}{\pi} \int_{-\pi}^{+\pi} d\phi \, B_{\text{Fourier}}(q, \phi; N) \cos(n\phi), \quad (3.15b)$$

$$\beta(q, 2n+1; N) = \frac{1}{\pi} \int_{-\pi}^{+\pi} d\phi \, B_{\text{Fourier}}(q, \phi; N) \sin(n\phi), \quad (3.15c)$$

where $n = 1, 2, \ldots, N$. Approximate values of the coefficients can be obtained by replacing $B_{\text{Fourier}}(q, \phi; N)$ by the measured magnetic field strengths and by replacing the integrals with finite sums that approximate the integrals. This method, which is analogous to numerical integration methods, has an obvious weakness that the samplings in ϕ are limited to the points at which the measurements were made. Therefore, accuracies of the Fourier coefficients that are computed by using this method deteriorate as n approaches the sampling rate of the data. A further drawback to this method is that it couples the issue of the numerical accuracy of the Fourier coefficients to the issue of the stability of the Fourier coefficients with increasing N, making it difficult to assess the latter.

The method we employ to determine $B_{\text{Fourier}}(q, \phi; N)$ is a least-squares fit. That is, we find the minimum of

$$\chi_q^2(N) = \frac{1}{N_\phi} \sum_i \left[\frac{B_{\text{measured}}(\zeta_q, \eta_q, \phi_i) - \langle B \rangle - B_{\text{Fourier}}(q, \phi_i; N)}{\langle B \rangle} \right]^2 \tag{3.16a}$$

$$= \frac{1}{N_\phi} \sum_i \left[\frac{B_{\text{measured}}(\zeta_q, \eta_q, \phi_i) - \langle B \rangle - [\partial B_{\text{Fourier}}(q, \phi_i)/\partial \beta(q, n; N)] \beta(q, n; N)}{\langle B \rangle} \right]^2, \tag{3.16b}$$

where the sum is over all values of ϕ at which the measurements were made, and N_ϕ is the number of measurements.[6] In practice we solve this linear least-squares problem by making use of the SVD method. That is, we find the pseudoinverse of the matrix

$$\frac{\partial B_{\text{Fourier}}(q, \phi_i; N)}{\partial \beta(q, n; N)}, \tag{3.17}$$

whose indices are i and n, and apply it to the column vector $B_{\text{measured}}(\zeta_q, \eta_q, \phi_i) - \langle B \rangle e_i$, whose index is i. (Here e is a column vector with all unit entries.) We denote by $\chi_q^{\min}(N)$ the minimum value of $\chi_q(N)$:

$$\chi_q^{\min}(N) = \min_{\beta(q, n; N)} \chi_q(N). \tag{3.18}$$

We also define

$$\chi^2(N) = \frac{1}{N_{\text{probe}}} \sum_{q=1}^{N_{\text{probe}}} [\chi_q^{\min}(N)]^2. \tag{3.19}$$

It is obvious that the minimum of $\chi_q(N)$ will decrease with increasing N. Of course, this does not mean that we can increase N indefinitely. If N is too large, the Fourier coefficients become very sensitive to small fluctuations in data, which may be comparable to the uncertainties in measurement. Furthermore, the resulting Fourier series $B_{\text{Fourier}}(q, \phi; N)$ can exhibit unphysically large fluctuations at values of ϕ for which there are no data.

In order to deal with these issues, we use the following method to determine a value of N such that the Fourier series best approximates the actual magnetic field. We note that, if the Fourier coefficients are known exactly, then

$$\bar{\chi}^2(N, N') = \frac{1}{2\pi N_{\text{probe}}} \sum_{q=1}^{N_{\text{probe}}} \int_{-\pi}^{+\pi} d\phi \left[\frac{B_{\text{Fourier}}(q, \phi; N) - B_{\text{Fourier}}(q, \phi; N')}{\langle B \rangle} \right]^2, \tag{3.20}$$

---

[6]Note that the quantity $\chi_q^2(N)$ is *not* the usual quantity χ^2 that appears in statistics, as it is normalized to $\langle B \rangle$, rather than to the experimental error.

will decrease with decreasing $N - N' = \Delta N$ for fixed N, and also for increasing N with fixed ΔN, as long as N is large enough. We will apply these criteria to determine the optimal choice of N for the Fourier analysis. When we compute $\bar{\chi}(N, N')$, we make use of Parseval's theorem, which yields

$$\bar{\chi}^2(N, N') = \frac{1}{2N_{\text{probe}}} \sum_{q=1}^{N_{\text{probe}}} \left[\frac{2\left[\beta(q, 0; N) - \beta(q, 0; N')\right]^2 + \sum_{n=1}^{n_{\text{max}}} [\beta(q, n; N) - \beta(q, n; N')]^2}{\langle B \rangle^2} \right],$$

(3.21)

where $n_{\text{max}} = \max(2N + 1, 2N' + 1)$.

3.3.3 Constraining the toroidal-harmonic coefficients

Having determined the coefficients $\beta(q, n; N)$ of the Fourier series in ϕ for each probe, we can now complete the determination of the toroidal coefficients C_{CC}^{mn}, C_{CS}^{mn}, C_{SC}^{mn}, and C_{SS}^{mn}. (Recall that we denote these toroidal-harmonic coefficients by c_i.) Then we determine the c_i by minimizing the following quantities for each n:

$$\sum_q \left[\beta(q, 2n; N) - B_C(\zeta_q, \eta_q, n)\right]^2 \tag{3.22a}$$

$$= \sum_q \left\{\beta(q, 2n; N) - [\partial B_C(\zeta_q, \eta_q, n)/\partial c_i]c_i\right\}^2 \tag{3.22b}$$

and

$$\sum_q \left[\beta(q, 2n + 1; N) - B_S(\zeta_q, \eta_q, n)\right]^2 \tag{3.23a}$$

$$= \sum_q \left\{\beta(q, 2n + 1; N) - [\partial B_S(\zeta_q, \eta_q, n)/\partial c_i]c_i\right\}^2 \tag{3.23b}$$

where $B_C(\zeta_q, \eta_q, n)$ and $B_S(\zeta_q, \eta_q, n)$ are given by eq. (3.13).

Again, we use the SVD method. We find the pseudoinverses of the matrices

$$\frac{\partial B_{C,S}(\zeta_q, \eta_q, n)}{\partial c_i}, \tag{3.24}$$

where the matrices have indices i, which runs from 1 to $2M + 1$, and q, which runs from 1 to N_{probe}. We apply the pseudoinverse of the "C" matrix to the column vector $\beta(q, 2n; N)$, which has index q; we apply the pseudoinverse of the "S" matrix to the column vector $\beta(q, 2n + 1; N)$, which also has index q. This linear least-squares problem is underconstrained, for the reasons that we discussed in section 3.2. Therefore, the SVD procedure is very convenient for finding a particular solution.

We must carry out this procedure for each of the $2N + 1$ Fourier components. However, the matrices in eq. (3.24) have dimensionality $(2M + 1) \times N_{\text{probe}}$, while the matrix in eq. (3.5b) that appeared in the original linear least-squares problem for the toroidal coefficients has dimensionality $(2M + 1)(2N + 1) \times N_{\text{data}}$. Consequently, the determination of the c_i in this step requires much less computational time than does the determination of the c_i directly from the original least-squares problem.

In the current $g - 2$ experiment, N_{probe} is either 17 or 25. This number is not sufficiently large to allow us to use the analogue of $\bar{\chi}(N, N')$ in eq. (3.20) to determine the optimum value for the number of poloidal terms M in the toroidal harmonic series. Instead, we vary M over a range of 5–8 for the case of 25 probes and check to see if there are noticeable differences in the predictions of the toroidal-harmonic series for $\mathbf{B}$.
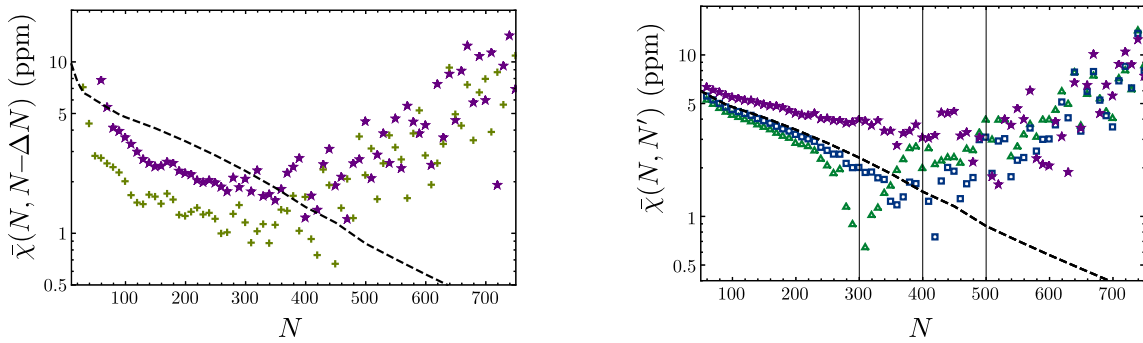
Figure 2. Values of $\bar{\chi}(N, N')$ for the data of Run 52. The left figure shows $\bar{\chi}(N, N - \Delta N)$ in units of ppm, as a function of N, with ΔN fixed to 20 and 50 (shown with crosses and stars, respectively). The right figure shows $\bar{\chi}(N, N')$ in units of ppm, as a function of N, with N' fixed to 300, 400, and 500 (shown with triangles, squares, and stars, respectively). In both figures, the dashed line indicates the values of $\chi(N)$ [eq. (3.19)] in units of ppm.

4 Application of the toroidal-harmonic method to data

In this section, we demonstrate the toroidal-harmonic method that we have described by applying it to magnetic-field data from the $g - 2$ experiment. In these applications, we take $\langle B \rangle$, expressed in units of the NMR frequency, to be 61.8 MHz. We take the tolerance in the SVD calculations of the toroidal coefficients to be $\epsilon = 10^{-8}$. We have found that varying ϵ over several orders of magnitude makes very little numerical difference in the gradients of the magnetic field that are well constrained by Maxwell's equations.

We emphasize that the results that we present are for illustrative purposes only. These results are based upon data that were taken early in the commissioning of the muon-storage-ring magnetic field, and they data do not reflect either the quality of the magnetic field or the quality of the magnetic-field measurements that will ultimately be used in the experiment.

4.1 Fourier decomposition

First we show results from the Fourier decomposition in ϕ of the data from each probe.

4.1.1 Run 52 data

We begin by examining data from trolley Run 52 (ref. [15]), which are based on measurements from 25 NMR probes (located in the "shimming trolley") at 7842 azimuthal angles, for a total of 196050 data points.

In figure 2, we show the quantity $\bar{\chi}(N, N')$ [eq. (3.20)]. As can be seen from both of the plots in this figure, the quality of the Fourier decomposition is optimal around $N = 300$. We note that $\chi(N)$ continues to decrease beyond $N = 300$. However, the plots of $\bar{\chi}(N, N')$ and $\bar{\chi}(N, N - \Delta N)$ indicate that the fits become unstable when N becomes significantly greater then 300. This instability manifests itself in large changes in the low-order Fourier coefficients and in unphysically large fluctuations in the values of the truncated Fourier series at points that lie between the data points. Therefore, we choose $N = 300$ in our fits, which implies that there are 601 Fourier components in our Fourier analysis of the ϕ dependence for each probe. We have carried out the computation of
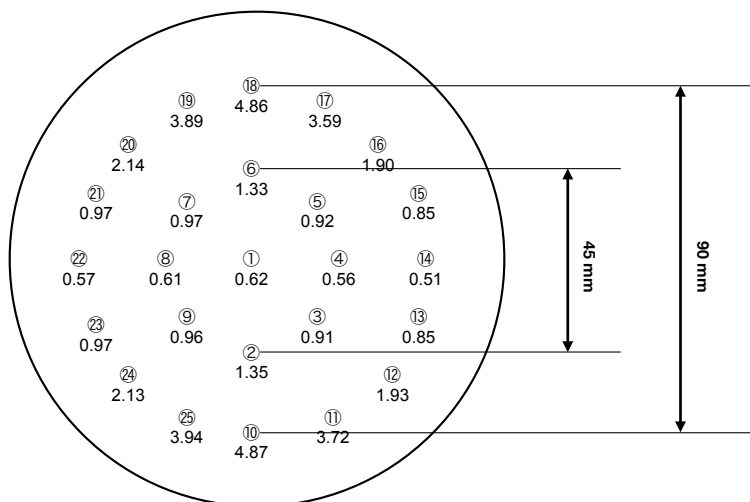
Figure 3. Approximate positions in the ρ-z plane of the NMR probes in the 25-probe trolley. The coordinate ρ increases as one moves to the right in the figure, and the coordinate z increases as one moves upward in the figure. The position of probe 1 is given by $\rho = 7112$ mm and $z = 0$ mm. Under each probe position, we list the value of $\chi_q^{\min}(300)$ in ppm that we have obtained for that probe from the Run 52 data.

the Fourier coefficients using Mathematica code [16]. In the Mathematica code, it is very important to vectorize the matrix operations, which results in about an order-of-magnitude reduction in the computational time and almost a factor of 2 reduction in the memory usage. The computation of the Fourier coefficients takes approximately 4 minutes on a dual 6-core 2.6 GHz Intel Xeon CPU system and consumes about 1.5 GB of memory in total.

Already, at the level of the Fourier analysis, the fit provides useful information about the field measurements. Figure 3 shows the approximate positions in the ρ-z plane of the 25 NMR probes. Under each probe position, we list the value of $\chi_q^{\min}(300)$ [eq. (3.18)] in ppm that we have obtained for that probe. First, we note that the values of $\chi_q^{\min}(300)$ that we have obtained are much larger than the nominal probe measurement uncertainty of 10 ppb. This suggests that there may be spatial variations in the magnetic field that are on too small a scale to be represented accurately by the fit, temporal variations in the magnetic field, and/or measurement anomalies in the data. We note that the values of $\chi_q^{\min}(300)$ display an interesting spatial distribution: $\chi_q^{\min}(300)$ is larger at the top and bottom of the trolley than in the middle and is fairly uniform across a given horizontal row. This may provide a clue as to the origin of the unexpectedly large values of $\chi_q^{\min}(300)$.

In figure 4, we show the distributions of residuals between the Fourier series fit and the data from Run 52 for probes 1 and 17. As can be seen, the widths of the distributions are rather different, as would be expected from the different values of $\chi_q^{\min}(300)$.

Figure 5 shows the Fourier series fit for probe 1 and probe 17, along with the data as a function of ϕ. These figures reveal significant deviations of the data from the fit, especially in the case of probe 17. One such deviation can be seen in the "zoomed-in" figure for probe 17 near 184°. There, the data appear to be smooth in the region of the deviation. However, the fit does not contain enough
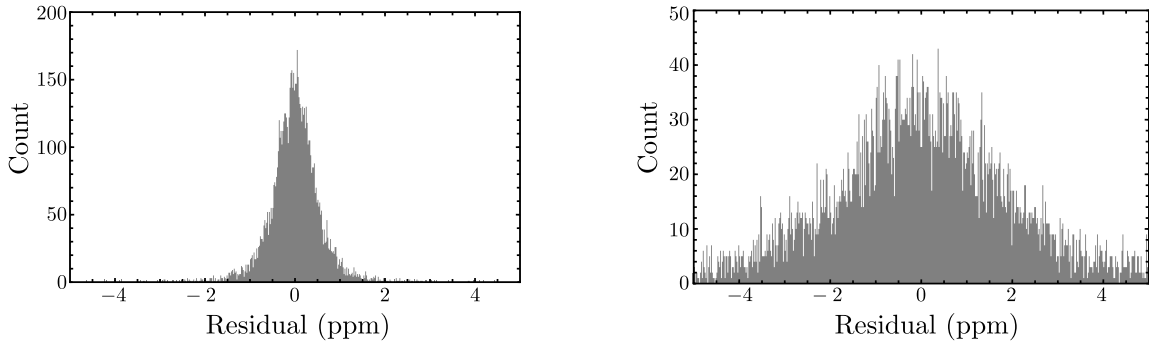
Figure 4. Residuals in ppm between the Fourier series fit and the data from Run 52 for probe 1 (left figure) and probe 17 (right figure).
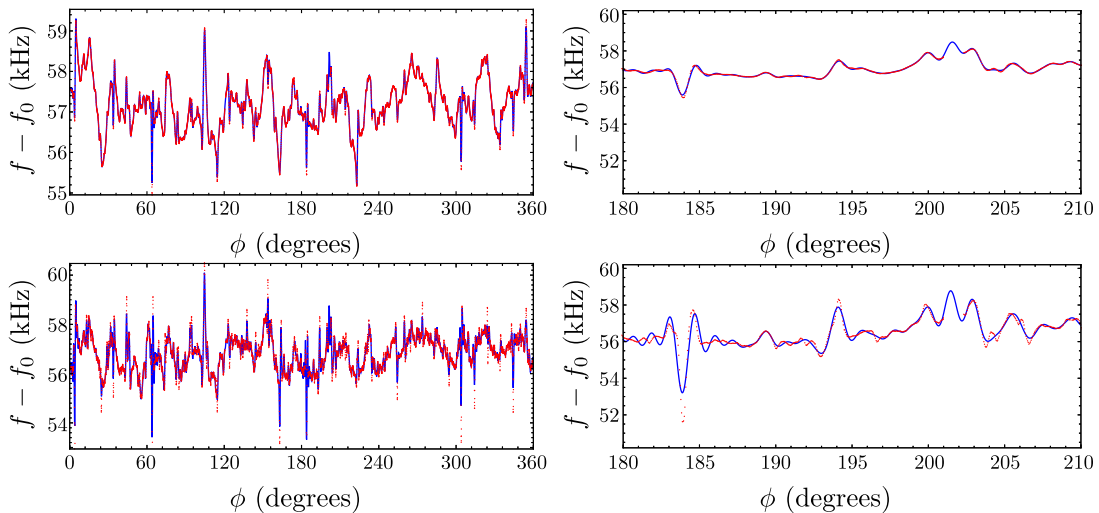

Figure 5. Fourier series fit and Run 52 data for probe 1 (upper figures) and probe 17 (lower figures). The figures on the left show the full range of ϕ; the figures on the right are "zoomed in" to a smaller range of ϕ. The points (red) are the data and the curve (blue) is the fit. The vertical axis is B_z in units of the NMR frequency, offset by an amount $f_0 = 61.74$ MHz. For these data, 1 ppm is approximately 0.062 kHz.

harmonics to follow the data accurately. It is not possible to increase the number of harmonics for this data set because, as we have mentioned, the fits become unstable as N increases beyond about 300. This instability can be traced to nonuniformity in the sampling of the data over the range of ϕ. For example, the gap in the measurements in the range $\phi = 201$–$202°$ can cause instabilities once N is sufficiently large for the harmonics to probe the gap because the fit function is completely unconstrained in the range of the gap. We would expect this $1°$ gap to produce instabilities when $N \sim 360°/1°$, which is in agreement with the stability analysis that is based on $\bar{\chi}(N, N - \Delta N)$ and $\bar{\chi}(N, N')$.

4.1.2 Run 3483 data

For comparison, we also show results from a later trolley run (Run 3483) in which the trolley contained 17 NMR probes. The data for this run [15] contain measurements at 9023 azimuthal angles, for a total of 153391 data points. In figure 6, we show the quantity $\bar{\chi}(N, N')$ [eq. (3.20)].
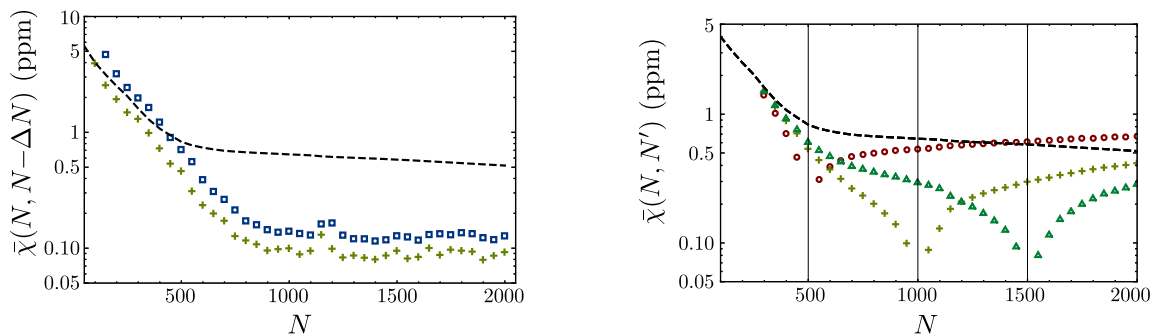
Figure 6. Values of $\bar{\chi}(N, N')$ for the data of Run 3483. The left figure shows $\bar{\chi}(N, N - \Delta N)$ in units of ppm, as a function of N, with ΔN fixed to 50 and 100 (shown with crosses and squares, respectively). The right figure shows $\bar{\chi}(N, N')$ in units of ppm, as a function of N, with N' fixed to 500, 1000, 1500 (shown with circles, crosses, and triangles, respectively). In both figures, the dashed line indicates the values of $\chi(N)$ [eq. (3.19)] in units of ppm.
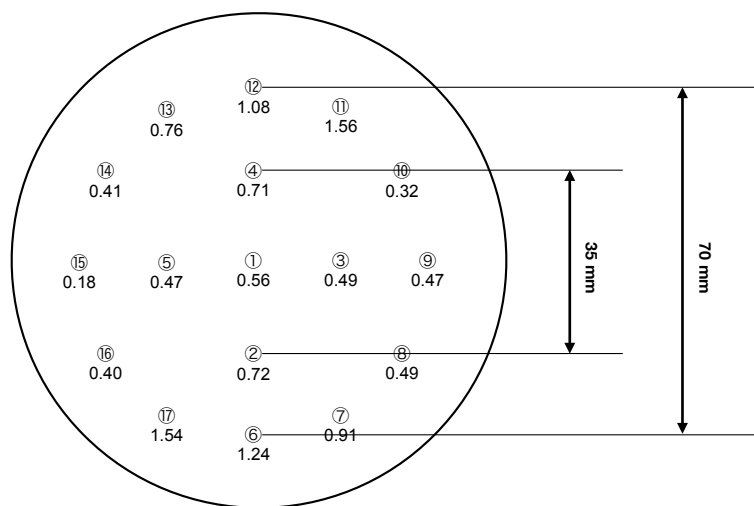

Figure 7. Approximate positions in the ρ-z plane of the NMR probes for the 17-probe trolley. The coordinate ρ increases as one moves to the right in the figure, and the coordinate z increases as one moves upward in the figure. The position of probe 1 is given by $\rho = 7112$ mm and $z = 0$ mm. Under each probe position, we list the value of $\chi_q^{\min}(500)$ in ppm that we have obtained for that probe from the Run 3483 data.

These figures show that $\chi(N)$ changes slope abruptly at $N = 500$, suggesting that most of the features of the data are reproduced by the fit at that value of N. Therefore, we choose $N = 500$ for our fits, which implies that there are 1001 Fourier components in our analysis of the ϕ dependence for each probe.

In figure 7, we show the approximate positions in the ρ-z plane of the 17 NMR probes. Under each probe position, we list the value of $\chi_q^{\min}$ [eq. (3.18)] in ppm that we have obtained for that probe. Again, the values of $\chi_q^{\min}(500)$ that we have obtained are much larger than the nominal probe measurement uncertainty of 10 ppb. However, they are smaller than the values of χ_q from
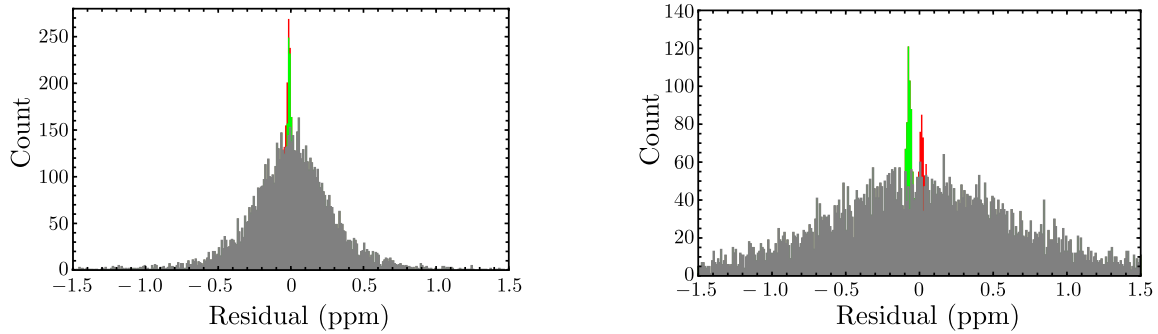
Figure 8. Residuals in ppm between the Fourier series fit and the data from Run 3483 for probe 1 (left figure) and probe 12 (right figure).

Run 52, perhaps reflecting an improvement in the uniformity of the magnetic field as a result of the shimming process. The values of $\chi_q^{\min}(500)$ display a spatial distribution that is similar to the spatial distribution of the values of $\chi_q^{\min}(300)$ from Run 52: The values of $\chi_q^{\min}(500)$ are larger at the top and bottom of the trolley than in the middle. However, the values of $\chi_q^{\min}(500)$ are less uniform across a given horizontal row than are the values of $\chi_q^{\min}(300)$ from Run 52.

In figure 8, we show the distributions of residuals between the Fourier series fit and the data from Run 3483 for probes 1 and 12. As was the case for the Run 52 data, the widths of the distributions are rather different. In this case, multiple approximately-Gaussian distributions are present. Two narrow distributions (shown in red and light green) arise from data in which multiple measurements were taken with the trolley in a particular azimuthal location. These distributions reflect the reproducibility of the measurements at a given trolley location as a function of time. A broader distribution (in gray) arises from data taken while the trolley was in motion, and may be indicative of actual field variations that are on too small a scale to be represented by the fit and/or measurement anomalies.

Figure 9 shows the Fourier series fit for probe 15 and probe 12, along with the data as a function of ϕ. In contrast with the corresponding figures for Run 52, these figures reveal the presence of large "spikes" in the data, for which a single measurement is significantly displaced from the adjacent measurements. These spikes are particularly apparent in the "zoomed-in" figure for probe 12 and, in general, they are much larger in the data for probe 12 than in the data for probe 15. This suggests that these spikes may be the reason for the large value of $\chi_q^{\min}(500)$ for probe 12. In the azimuthal direction, the smallest distance scale of any physical structure in the $g - 2$ ring is about 1 cm. Some of the spikes occur on a distance scale that is smaller than that, which suggests that they may be artifacts of the measurement, rather than features of the ring magnetic field. The idea that the spikes may be measurement artifacts is bolstered by the fact that the data for Run 52, which do not show spikes, were taken while the trolley was stationary, while the data for Run 3483, which do show spikes, were taken while the trolley was in motion.

4.2 Full toroidal-harmonic fit

Finally, we discuss the full toroidal-harmonic fit to the data, taking $M = 8$ poloidal terms for each Fourier harmonic. We have written Mathematica code to carry out the computation of the toroidal-harmonic coefficients. The computation of the coefficients for all of the Fourier harmonics
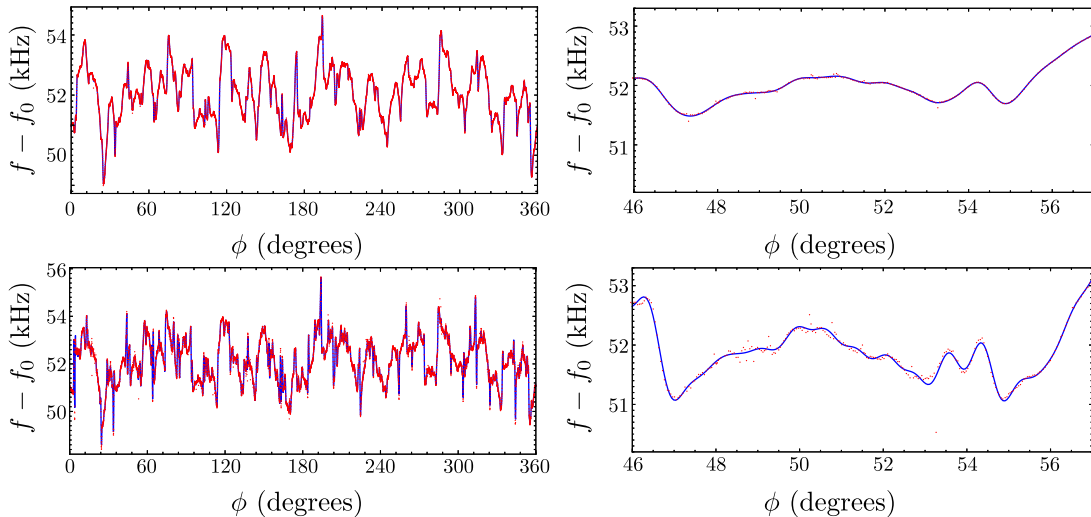
Figure 9. Fourier series fit and Run 3483 data for probe 15 (upper figures) and probe 12 (lower figures). The figures on the left show the full range of ϕ; the figures on the right are "zoomed in" to a smaller range of ϕ. The points (red) are the data and the curve (blue) is the fit. The vertical axis is B_z in units of the NMR frequency, offset by an amount $f_0 = 61.74$ MHz. For these data, 1 ppm is approximately 0.062 kHz.

takes approximately 6 minutes on a dual 6-core 2.6 GHz Intel Xeon CPU system and consumes less than 1 GB of memory in total.

In figure 10, we show Hall-probe measurements of the radial field component B_ρ and the predictions for B_ρ that come from our full toroidal-harmonic fit. (In contrast with the NMR probes, the Hall probes can resolve the individual magnetic-field components.) The data and the prediction are for Run 52 and correspond to an azimuthal angle $\phi = 167.229°$ and to a vertical line that passes through the center of the NMR-probe trolley.

The band in figure 10 shows our prediction for B_ρ from the full toroidal-harmonic fits to the Run 52 NMR-probe data. In estimating the uncertainties in the prediction, we use two measures of the quality of our fit. One is the rms deviation of the NMR measurements from the fit, as given in figure 3. The other is the stability of the fit with respect to changes in M. Specifically, the overall uncertainty in the band in figure 10 (thick lines) was obtained by adding in quadrature the following quantities: (1) a polynomial fit of order three to the rms deviations of the data from the fit that are shown in figure 3 and (2) the change in the fit that is obtained by varying M from 5 through 8 (thin lines in the band). In estimating the uncertainties, we are assuming that the physical field cannot vary rapidly in the z direction in the interval between probe measurements. This assumption is supported by the fact that the distance between probe measurements is considerably smaller than the distance scale of the physical structure in the z direction (the diameter of the $g-2$ vacuum pipe.)

A further source of error in the full toroidal-harmonic fits arises from the fact that the NMR trolley does not follow a perfect circle in the azimuthal direction. Rather, it is translated by amounts that are less than 2 mm in the radial direction and less than 1.5 mm in the vertical direction [17]. The characteristic azimuthal angle over which these translations occur is about 10°. The displacements of the trolley NMR probes that arise from rotations are much less than the displacements that arise from translations. Consequently, the main effect of deviations of the trolley motion from purely
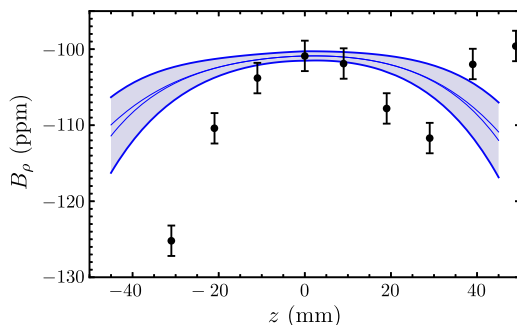
Figure 10. The radial field component B_ρ at $\phi = 167.229°$. Filled circles: Hall-probe data for the Run 52 field configuration. Band: results from the full toroidal harmonic fit to the Run 52 data, with value at $z = 0$ mm adjusted to match the Hall probe data. The uncertainties that are shown in the band and for the filled circles are discussed in the text.

circular motion is to translate the field coordinates from their true positions. Since the characteristic azimuthal angle over which these deviations occur is much larger then either the distance between azimuthal measurements or $2\pi/N$, the fits should be able to follow easily these overall translations as a function of azimuthal angle. Therefore, the trolley translations are not expected to have a significant affect on the χ^2/d.o.f of the toroidal-harmonic fits. The translations, of course, do not affect the gradients of B_z, and, so, do not affect the constraints that are implied by Maxwell's equations (3.9) or the results in figure 10. Examinations of the full toroidal-harmonic fits and the raw NMR data both indicate that the B_z field gradients range from about 0.8 ppm/mm near the outer probes to about 0.11 ppm/mm near the inner probes. Therefore, we expect the errors from overall translations to be less than about 2 ppm near the outer probes and less than about 0.28 ppm near the inner probes. These errors could be corrected by translating the coordinates of the fields that are obtained from the toroidal harmonic fits by the measured amounts of the trolley translations.

The points in figure 10 show the Hall-probe data for B_ρ at $\phi = 167.229°$ for the Run 52 magnetic-field configuration [2]. The nominal uncertainties in the Hall-probe measurements are 1–2 ppm. We show 2 ppm error bars in the figure.

We stress that, in the toroidal-harmonic fit, only $\partial B_\rho/\partial z$ is constrained, and so only the shape of the curve for B_ρ is meaningful. As can be seen on comparison of the fit results with the Hall-probe data, there is considerable tension between the shapes. The data points at displacements of -3, $+3$, $+4$, and $+5$ cm from the central position were taken in different sessions than were the more central data points, and so some offsets may have occurred. However, even the more central data points show much larger displacements as the distance from center is varied than does the fit. The tension between the prediction and the measurements may indicate that there is an, as yet, unknown systematic uncertainty at play in the Hall-probe measurements.

The main effect of the transverse fields in the $g-2$ measurement is to induce oscillations of the beam in the transverse direction. The Hall-probe measurements serve as an independent check of the direct measurements of the transverse beam oscillations. The discrepancies between the Hall-probe measurements and predictions from Maxwell's equations that are shown in figure 10 are smaller than the uncertainties in the values of the transverse fields that can be deduced from the measurements of the beam oscillations. Hence, these discrepancies would not be expected to

be important in the $g - 2$ measurement. However, they may be more significant for the proposed measurement of the electric-dipole moment of the muon.

5 Summary

In this paper, we have presented a method for incorporating the constraints that are imposed by Maxwell's equations into fits to the NMR-probe data for the magnetic field of the $g - 2$-experiment storage ring. Maxwell's equations are enforced in the fits by making use of a fitting function that consists of a truncated series of toroidal harmonics. The toroidal harmonics are expressed as functions of toroidal coordinates, which are well suited to the storage-ring geometry.

The NMR probes measure the magnitude of the magnetic field, rather than its individual components. It would be impractical to fit the toroidal harmonic series for the magnitude of the magnetic field to the data because the fitting problem is highly nonlinear and because the transverse magnetic-field components (components that are transverse to the average field direction) are not fully determined from the magnitude of the field in combination with Maxwell's equations. Therefore, we have simplified the fitting procedure by approximating the magnitude of the field by its principal (vertical) component. Given that the transverse components of the magnetic field in the $g - 2$ storage ring are typically of order 100 ppm, the corrections to this approximation are of order 0.01 ppm, which is comparable to the nominal error in the NMR-probe measurements.

Even this linear fitting problem is difficult computationally. Difficulties arise because of the large number of data points (of order 10^5), the large number of toroidal harmonics that is required for an accurate fit (of order 10^4), and the fact that the fit does not fully constrain the coefficients of the toroidal harmonics. A further difficulty is that the data display fluctuations between measurements at different azimuthal angles that are much larger than the differences between the measurements of the various probes at a fixed azimuthal angle. In order to ameliorate these problems, we further rearranged the fitting procedure in to two steps. First, we fit the azimuthal dependence of the measurements of each probe to a truncated Fourier series. Then, we used the Fourier series coefficients for all of the probes to determine the coefficients of the toroidal harmonics. The underconstrained nature of the problem is confined essentially to this second step, which involves a fitting problem whose dimensionality is much lower than the dimensionality of the original linear fitting problem. We deal with the underconstrained nature of the problem by using the singular-value decomposition (SVD) method, which identifies and isolates the underconstrained modes. This modified fitting procedure results in a very efficient computational algorithm that is easily carried out on a present-day desktop computer.

We have used this method to fit some of the early NMR-probe data that were taken by the $g - 2$ collaboration. While these data are not representative of the magnetic-field homogeneity or the field-measurement precision that will ultimately be used by the $g - 2$ collaboration to make the $g - 2$ measurement, they serve to illustrate some of the features of the fitting procedure.

Even at the level of the fits to the truncated Fourier series, it is apparent that the deviations of the data from the fit are much larger than the nominal precision of the NMR-probe measurements. Such fits may be useful in diagnosing sources of uncertainties in real-world field measurements. The full fits to the truncated toroidal-harmonic series are in tension with Hall-probe measurements

of the radial component of the magnetic field, suggesting that there may be systematic errors in the Hall-probe measurements that are not yet understood.

We expect that the toroidal-harmonic fits will continue to be a useful tool in understanding the magnetic-field measurements in the $g - 2$ storage ring as those measurements evolve. The toroidal-harmonic fits may be even more important for the planned muon electric-dipole-moment measurement. That measurement may be more sensitive than is the $g - 2$ measurement to the transverse components of the magnetic field. Those components are not easy to access by direct measurements, and so the information about them that can be gleaned from Maxwell's equations could be particularly valuable.

Acknowledgments

References

[1] E989 collaboration, *Muon g − 2 technical design report*, http://lss.fnal.gov/archive/design/fermilab-design-2014-02.pdf.

[2] R. Osofsky, private communication.

[3] W.M. Hicks, *On toroidal functions*, *Phil. Trans. Roy. Soc. London* **172** (1881) 609.

[4] A.B. Basset, *On toroidal functions*, *Amer. J. Math.* **15** (1893) 287.

[5] B. van Milligen and A.L. Fraguas, *Expansion of vacuum magnetic fields in toroidal harmonics*, *Comput. Phys. Commun.* **81** (1994) 74.

[6] A. Kuznetsov and S. Shchepetov, *Method of magnetic analysis for stellarator equilibria*, *Nucl. Fusion* **37** (1997) 371.

[7] Y. Fischer, *Identification de paramètres magnétiques à l'intérieur d'un tokamak* (in French), hal-00679835, (2012).

[8] L. Gambini, *Expansion of the magnetic flux density field in toroidal harmonics*, Master thesis, CERN-THESIS-2018-040, Bologna U., Bologna, Italy (2018).

[9] M. Abramovitz and I. Stegun, *Handbook of mathematical functions*, U.S. Government Printing Office, Washington, DC, U.S.A. (1972).

[10] C.L. Lawson and R.J. Hanson, *Solving least squares problems*, Society for Industrial and Applied Mathematics, Philadelphia, PA, U.S.A. (1995).

[11] E.H. Moore, *On the reciprocal of the general algebraic matrix*, *Bull. Amer. Math. Soc.* **26** (1920) 394.

[12] A. Bjerhammar, *Application of calculus of matrices to method of least squares, with special references to geodetic calculations*, *Trans. Roy. Inst. Tech. Stockholm* **49** (1951) 1.

[13] R. Penrose, *A generalized inverse for matrices*, *Math. Proc. Cambridge Phil. Soc.* **51** (1955) 406.

[14] R. Penrose, *On best approximate solutions of linear matrix equations*, *Math. Proc. Cambridge Phil. Soc.* **52** (1956) 17.

[15] J. Grange, R. Hong and P. Winter, private communication.

[16] Wolfram Research Inc., *Mathematica*, version 11.3, Champaign, IL, U.S.A. (2018).

[17] P. Winter, private communication.